Medical Research Archives

ESMED
European Society of Medicine

OPEN ACCESS

Published: September 30, 2022

Citation: Righi M, Morara S, et al., 2022. A Spatial Dispersion Approach Qualifies to Quantify Vascular Alterations in a Swine Amyotrophic Lateral Sclerosis Model, Medical Research Archives, [online] 10(9). https://doi.org/10.18103/mra.v10i9.3152

DOI
https://doi.org/10.18103/mra.v10i9.3152

ISSN: 2375-1924

RESEARCH ARTICLE

A Spatial Dispersion Approach Qualifies to Quantify Vascular Alterations in a Swine Amyotrophic Lateral Sclerosis Model

Marco Righi[1,2,*], Stefano Morara [1,2], Giulia Petrillo [1,2], Andrea Perota[3], Giulia Cagnotti[4], Cristiano Corona [5].

1. CNR - Institute of Neuroscience, Milan, Italy
2. NeuroMI, Milan Center for Neuroscience, University of Milano Bicocca, Milan, Italy
3. Laboratory of Reproductive Technologies, Avantea, Cremona, Italy
4. Department of Veterinary Science, University of Turin, Grugliasco, Italy.
5. Istituto Zooprofilattico Sperimentale Piemonte Liguria e Valle d'Aosta, Turin, Italy.

* marco.righi@in.cnr.it

ABSTRACT

Amyotrophic Lateral Sclerosis is still a poorly understood neurological syndrome showing muscle impairment and leading to death because of respiratory failure. Recently, a new, transgenic swine model overexpressing the human superoxide-dismutase 1 gene, promised the chance to investigate animals before disease onset, and we planned to investigate vascular alterations that we recently learned to quantify. In order to address for feasibility, we checked angioarchitectures in spinal cord samples of at least one animal for each of three health conditions: healthy, asymptomatic, clear motor symptoms. Furthermore, analyses were carried out in three different regions: cervical, thoracic and lumbar districts.

In our approach, we relied on described ImageJ automatic routines, measuring amounts and dispersion of microvascular structures, classified according to their calibers and in spite of the low height of the sample slice. As in previous papers, we investigated amount and volume dispersion of 7 progressively reconstructed angioarchitectures, built from larger calibers through addition of vessels or voxels of smaller and smaller caliber. Results were processed by linear regression to depict a 2D summary pattern, specific for that micro-angioarchitecture.

Healthy samples presented well dispersed vascular layouts, depicted by near-flat linear regressions. However, they were characterized by large dispersion variances, apparently due to district of origin of the sample itself. On the contrary, results from pathological samples presented lines with increased slopes while retaining the observed inter-sample dispersion variances. Absence of samples from different animals in the same health status prevented us to observe inter-animal variances. Therefore, we could not derive significant biological conclusions on reduced vascularization. Nevertheless, results demonstrated the success of our image analysis approach and provided a "tantalizing" observation of vascular alterations in a swine model for Amyotrophic Lateral Sclerosis.

Introduction

Amyotrophic Lateral Sclerosis (ALS)[1] is an adult-onset neurodegenerative disorder affecting both upper and lower motor neurons. Although slowly progressing, ALS is fatal because of respiratory failure due to motor neuron loss and impairment.

Human genetic analyses revealed that mutations in the gene coding for the antioxidant enzyme Cu, Zn-superoxide dismutase 1 (SOD1) occur in 10%–20% of familial ALS cases. The importance of these mutations is reduced in sporadic ALS[2,3], but still they contribute to up to 7% the total number of patients. Pathogenesis is thought to be due to a gain of function for SOD1, at least in the transgenic rodents expressing the mutant human SOD1 gene (hSOD1)[4]. Further researches contributed to the discovery of other pathogenetic mechanisms underlying the disease, including defects in axonal transport[5], oxidative stress[6,7], protein misfolding[3,7], mitochondrial dysfunction[7], excitotoxicity[8,9] and altered RNA metabolism[10,11]. However, they failed to unravel the main culprit, a hidden actor and mechanism starting the avalanche of dysfunctions.

From the clinical point of view, rodent models lack a specific pre-symptomatic period that can be observed in ALS patients but not in diseased mice[12]. Additional animal models are therefore required, and some of us recently described a transgenic swine model expressing hSOD1 and recapitulating most of the clinical human symptoms[13]. Hallmark of this model is the possibility to study the long (27 months) pre-symptomatic period in which transgenic pigs accumulate system dysfunctions, but lack clinical manifestations[14]. This clinically silent interval is thought to be due to intrinsic reserves within the neuromuscular system or to transitory activation of compensatory mechanisms[15,16]. At the end of the pre-symptomatic period, developing neurological symptoms lead to the death of the animal in up to some months, according to transgene copy numbers.

Very recent genetic data in human sporadic ALS revealed perivascular fibroblast alterations[17] as one of the initial markers of the disease, even before microglia activation[18]. This finding confirms other observations[19,20] related to subtle alterations in blood vessels, and demanded for a detailed investigation, switching research on pathogenesis to new mechanisms. This aspect was so far disregarded because of the very complex task required by the representative description of a microangioarchitecture. Actually, vessel classification according to dimensions[21], tortuosity[22,23], splitting points[21], provide only descriptive values which is difficult to turn into a representative parameter, specific for that angioarchitecture. Even the use of fractals[24,25] added new insights, but was not conclusive.

In spite of these difficulties, it is well known that in many neurodegenerative diseases neurological alterations progress along with vascular alterations, as it occours in retinal blood plexa[26]. This observation is now widely accepted for Alzheimer's[27], diabetes[28], Parkinson Disease[29] and Multiple Sclerosis[30] and might provide a turning point in the study of these pathologies.

Given this context, one of us[31] recently demonstrated the possibility to recapitulate vascular alterations into quantitative parameters, after treatment of an angioarchitecture by anti-angiogenic or anti-vascular drugs. This semi-automatic image analysis study was performed in xenotransplanted mice carrying human multiple myeloma cells[32]. The same analytical approach was used to quantify the extent of vascular alterations observed in the brain of the *twitcher* mouse[33,34], an accepted animal model of human Krabbe Disease[35]. On a more technical ground, these studies were so far favored by tissue accessibility and easy vascular identification. Here, we challenged these conditions trying to extend this approach to the study of spinal cords in an ALS swine model[14]. In this preliminar study, we tested the usefulness of our quantitative approach; we observed tiny, repeatable differences in angioarchitectures, according to sampled spinal cord districts. Therefore, spatial dispersion of caliber-classified vessels seems an appropriate approach for a large scale analysis of this animal model of ALS.

Methods

Animal production

All procedures were conducted as described by the institutional guidelines that are in accordance with national (D.L. no. 116, G.U. suppl. 40, February 18, 1992, no. 8, G.U., 14 luglio 1994; D.L.26/2014) and international laws and policies (EEC Council Directive 86/609, 63/2010, OJ L 358, December 12, 1987; National Institutes of Health Guide for the Care and Use of Laboratory Animals, US National Research Council, 1996). hSOD1G93A Tg pigs were produced as previously reported[36].

Sample acquisition

Pigs were sacrificed according to the approved protocol of animal welfare[14]. Brain and spinal cord were rapidly dissected out and 4% PFA

immersion-fixed for immunofluorescence analysis. Tissues were then crioprotected in 30% sucrose and OCT embedded, respectively.

Thick frozen spinal cords (cervical, thoracic and lumbar segments) were cut in the coronal plane through a cryostat. The cut was made at a temperature that, at blade level, was between -27 and -25 °C. The sections obtained after cutting were collected in a 24 wells plate filled with cold 1x-PBS and Sodium azide 0,01% and kept in ice.

Vessel imaging and identification

Brain slices were transferred in a 48 wells plate in 1x-TBSx (0,1 M TRIS Base, 0,9% NaCl and 0,0125% TritonX-100) for 2 hour for medium equilibration. The solution was completely removed and sections were incubated with 400 µl of pre-incubation medium (10% Normal Serum and 2% BSA in 1x-TBSx) over night. The sections were subsequently incubated with 400 µl of Lycopersicon Esculentum (Tomato) Lectin DyLight 594 (Vetor Labs; diluted 1:1000 in 1x-TBSx) for 4 days. Sections were then rinsed 4x15 minutes with 1x-TBSx and 1x15 minutes with 1x-PBS. DAPI solution (1:25000, diluted in 1x-PBS) was applied for 1 hour in the dark. After rinsing 4x15 minutes with 1x-PBS, sections were then placed on microscope slides, completely covered with Vectashield mounting medium (Vector Labs) and slides were sealed with coverslips. Slides were kept at 4°C until imaging with confocal microscope. All steps were performed in 48 wells plate (1 slice per well) at room temperature on a tissue rocker.

Images were analysed with Zeiss LSM 800 confocal microscope using a 20x objective. Z-stacks were taken for each section using 1 µm intervals between each scan. Tomato lectin binding sites are widely expressed in all brain vessel types[37] and allowed to analyze the whole angioarchitecture of the spinal cord sections. Our analysis was focused on areas of spinal cord ventral horns that surrounded motoneurons, the prominent degenerating elements in ALS. Recovered images were nearly isotropic and could be processed without preliminary scaling. Isotropic voxel side was nearly 1.0 µm.

Automatic binary representation of vascular microangioarchitectures

Images were processed through the NIH Fiji/ImageJ application[38] v. 1.53a, on an Apple MacPro computer equipped with a 2.8-GHz Quad-Core Intel Xeon processor. Additional tools included the TransformJ plugin, freely available from ImageScience.org (https://imagescience.org/meijering/software/transformj/) and now incorporated into newer Fiji/ImageJ versions. Similarly, we used the appropriate Bio-Formats ImageJ plugin (https://docs.openmicroscopy.org/bio-formats/) to open .czi images. Our own ImageJ macros and plugins are detailed in this article and are available for download, as source code, searching for "*nHv95/Sclerotic_Analysis*" at the GitHub repository (https://github.com). They will be also available from the Corresponding Author on a reasonable request.

Starting from sample folders, automatic processing of fluorescent images to binary images was carried out using our ImageJ routine a-binaryStacks.txt. It started transforming 512x512x46 µm, .czi files into more common .tiff greyscale stacks using the quoted Bio-Formats plugin. They were saved inside a container target folder in a subfolder named according to sample, as signal (Red) and neuronal autofluorescence (Green) values. Given large differences in both signal intensity and background noise according to stack depth, we obtained further information using a 5 slices local projection algorithm rolling along the z-axis. The projected signals were further used to subtract a mediated background noise. This newly built stack was used as a mask to validate binary signals obtained from the original Red and Green channels after using default binary ImageJ algorithms and subtracting neuronal autofluorescence from vascular signals. Overall, our initial ImageJ macro transformed nearly-isotropic greyscale input images into binary stacks showing filled vessels, ready to allow for appreciation of caliber cross-sections.

Choice of microvascular calibers for vascular quantification

Filled vascular maps underwent voxel classification according to specific vascular calibers. This step was carried out by means of script b-classifyVessels.txt based on the area of the minimal vascular cross-section passing through a voxel, after considering cross-sections in the three Euclidean planes. Voxels were assigned to different classes of calibers based on arbitrary sets of area thresholds. Practically, we tested 3 set of thresholds defining these lowest classes: set A: 0-16vx, set B: 0-8vx and set C: 0-4vx. Each upper limit was serially multiplied by factor: 1.5, for set A; 1.7 set B; 1.9 set C, to define 7 caliber classes with minimal approximations. They covered calibers with cross-sections from 1-182vx, for set A; 1-193vx, for set B; 1-188vx, for set C. To choose the set to use, we

tested 6 different stacks obtained from a healthy animal; each set of thresholds was used to prepare samples that were then analyzed on a set-of-threshold basis, following the procedure described in the following paragraphs. Set A was selected and appeared to group cross-sections according to the following values: 0-16, 17-24, 25-36, 37-54, 55-81, 82-122, 123-182 voxels. Only this set of thresholds was used for the analyses of all the remaining samples.

Analysis of progressively reconstructed angioarchitectures

Following calibration, we used custom ImageJ macro c-oriSignals.txt which removed all signal voxels not present in original binary images, without affecting caliber classification of remaining signals. Then, voxels belonging to the largest class of calibers were combined with those from lower and lower classes using our custom ImageJ routine d-buildPRA.txt. This step builded a set of Progressively Reconstructed Angioarchitectures (PRA) for each vascular stack. Starting from larger calibers, PRA grouped voxels with calibers: 123-182 vx, 82-182 vx, 55-182 vx, 37-182 vx, 25-182 vx, 17-182 vx and 0-182 vx excluding only signals shown to belong to larger cross-sections.

Before analysis, all samples were normalized in order to compare angioarchitectures according their initial percent amount of signal voxels. It regarded all of the 6x3=18 (0-182 vx) PRA derived from the 6 samples, obtained from each of the 3 animals tested. The normalizing PRA was defined as the one showing the largest ratio between signal amount and whole sample volume. This step was performed using our ImageJ routine e-normalVolume.txt which calculated the amount/volume ratios from the involved PRA (0-182 vx) searching each sample folder. The elected image stack was duplicated by hand and added to each set of the remaining (*i. e.* 17) less populated stacks, on exclusive charge of the human operator. It is important to stress that normalization is specific for each analysis and must be repeated upon addition of new samples.

As a final step in this sample analysis, all 143 PRAs were processed using a custom ImageJ plugin compiled from our f-Spatial_Dispersion.java code[39]. This plugin calculated percent signal amount and spatial dispersion for each PRA in a set, repeating the task for all samples found in a source folder, and writing specific Result files. Spatial dispersion was assessed as the raw or normalized number of rhombicubocthahedron expansion cycles required to fill up a pre-determined amount of total volume, starting from signal voxels. Results reported both raw (Hv) and normalized (nHv) values for a volume fill-up of at least 90%, 95%, or 99%. As in previous works[31,39,40], we calculated spatial dispersion using index nHv 95%.

Statistical Analyses

Statistical analyses were performed using the statistical package Prism 5 (GraphPad Software, San Diego, CA, USA) run on an Apple Macintosh Pro personal computer. It helped drawing plots and graphical images as well as for Linear Regressions (LR). These lines were calculated using points from all the samples belonging to a specific condition, using program specifications. Fitness of LR was calculated by R^2 index but was not reported. When possible, each LR reported also its 95% confidence limits.

Results

Acquisition of spinal cord micro-angioarchitectures

Samples were acquired from spinal cords of 3 animals sacrificed at different times. Whereas control and symptomatic samples were obtained from animals aged 30 months, the pre-symptomatic animal was sacrificed at the end of its 20 months of age after careful consideration of its apparently normal health status. Unfortunately, matched age controls could not be analyzed.

Automatic binary representation of vascular micro-angioarchitectures

Upon transformation into usual greyscale stacks, fluorescent images showed variable intensities. In addition, vascular signals appeared corrupted by background noise and sporadic cellular autofluorescence (Figure 1, panel A). This was due to the fixation procedure (immersion fixation) originally employed to allow for recovery of unfixed but precious biological material, from a test animal. In order to cope with these difficulties, we wrote an ImageJ routine providing a rolling contrast enhancement based on the local projection of up to 5 surrounding slices. This procedure, coupled with controlled contrast enhancement and background/autofluorescence subtraction, provided acceptable results and identification of vascular wall signals which were highlighted in binary images (Figure 1, panel B). This important step did not however guarantee by itself the success of our analysis. In these analytical conditions, we were concerned by the small thickness of spinal cord samples with respect to previously tested isotropic neuroangioarchitectures[33] (Figure 1, see panels A' and C).

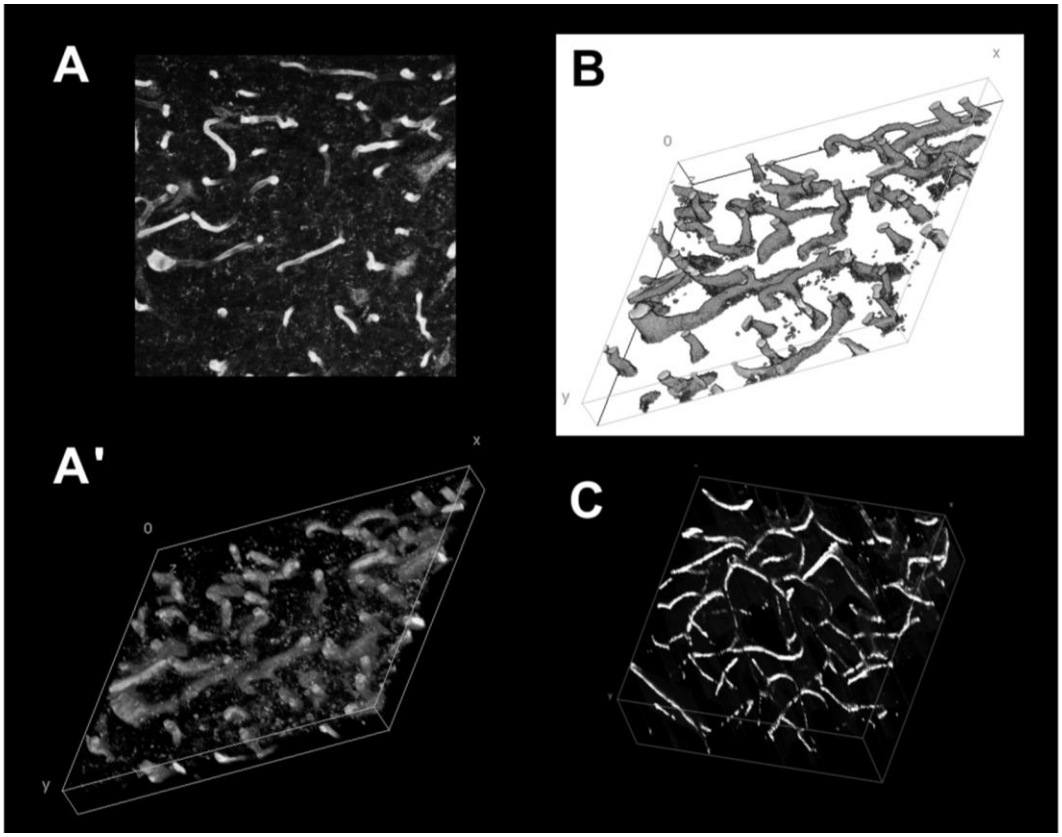

Figure 1 - Recovery of vascular signals. Panel **A**, Top: presents a z-projection, sum slice view of a spinal cord slice, stained by tomato lectin. Note cellular autofluorescence. **A'** Bottom: signals from the same slice are presented as a rendering view. Panel **B**: volume view of recovered binary voxels ready to be calibrated and used for analysis. Panel **C**: different geometry of a brain sample used for analysis of twitcher mouse vascularization[33].

Choosing appropriate thresholds for caliber classification

One of the limits of the original method[31,40] we were trying to adapt to the study of ALS is related to the need to calibrate vascular voxels, according to their vascular calibers. To cope with this need, hollow vessels had to be filled; then caliber of each signal voxel was calculated as the area of the minimal vascular cross-section in the 3 euclidean planes passing through the voxel itself[40]. This approach allowed to center analysis to small vessels, but demanded to define arbitrary thresholds to define all caliber classes to be used for analysis. To check for the importance of these parameters, we defined and tested 3 different sets of thresholds focused around the 0-180 vx area interval. The analysis was performed on a single stack from a control animal and results are shown in Figure 2. Set A presented the widest lower class of calibers (0-16vx), but it was set C to group largest calibers in a 99-188vx class covering near half of the considered cross-sections. Set B grouped intermediate values, although covering calibers up to cross-sections of 193vx. Plots reported increasing signal amounts due to Progressively Reconstituted Angioarchitectures (see below) versus spatial signal dispersion. This last parameter was calculated through 3D custom Euclidean Distance Maps. Despite differences in thresholds, all sets reported similar data arranged in close Linear Regressions. However, because of a flatter slope (signalling greater homogeneity in vessel dispersion), we used thresholds from set A to define caliber classes for all analytical samples.

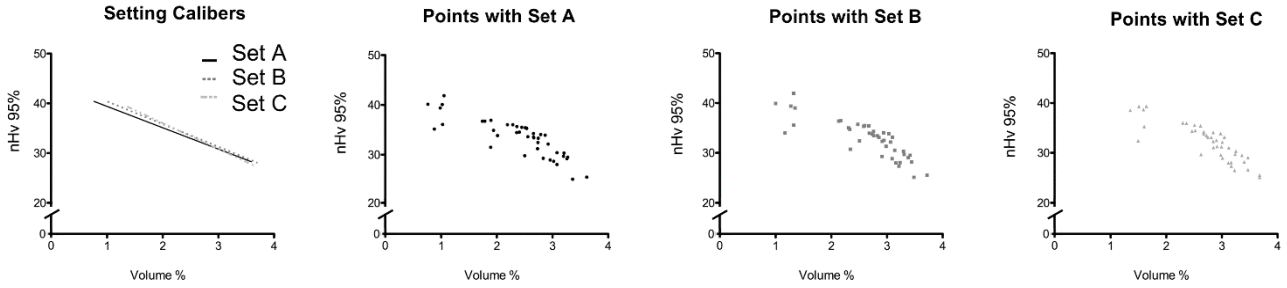

Figure 2 - Choice of caliber thresholds. Left panel presents linear regression lines obtained from an healthy cervical sample for 3 different Sets of calibers. Solid black line refer to Set **A**, dark grey to Set **B** and light grey to Set **C**. Following panels report position of data points for Set **A** to Set **C**. On the X axis the percent volume occupied by tested PRA. On the Y axis, plots present the normalized nHv95% index; i.e. the number of cycles needed to fill-up at least 95% of the total volume, by rhombicubocthahedron convolutions. Tested calibers: Set **A**: 1-182 vx. Set **B**: 1-193 vx, Set **C**: 1-188 vx.

Obtaining Progressively Reconstituted Angioarchitectures

The need to use PRAs as samples was stressed by previous findings[40], as isolated vascular signals belonging to different caliber classes do not provide simple clues about the overall microangioarchitecture from which they are obtained. Conversely, the approach we were adapting to the study of ALS wished to provide a defined answer: whether and how the initial pattern of larger voxels could be improved in terms of signal amount and 3D signal dispersion by addition of original vascular voxels from lower and lower calibers.

This approach was preferred in respect to a reverse one (smallest to largest), because only the former highlighted the increase in signal dispersion, taken as an indication of vascular pervasiveness. The number of PRAs to be tested (7) appeared to us as an acceptable compromise between speed and precision in LR calculation. PRA build-up was obtained automatically through an ImageJ routine after voxel classification. To exemplify process, Figure 3 reports the visual sequences of PRAs built from caliber classified signals for 3 different samples.

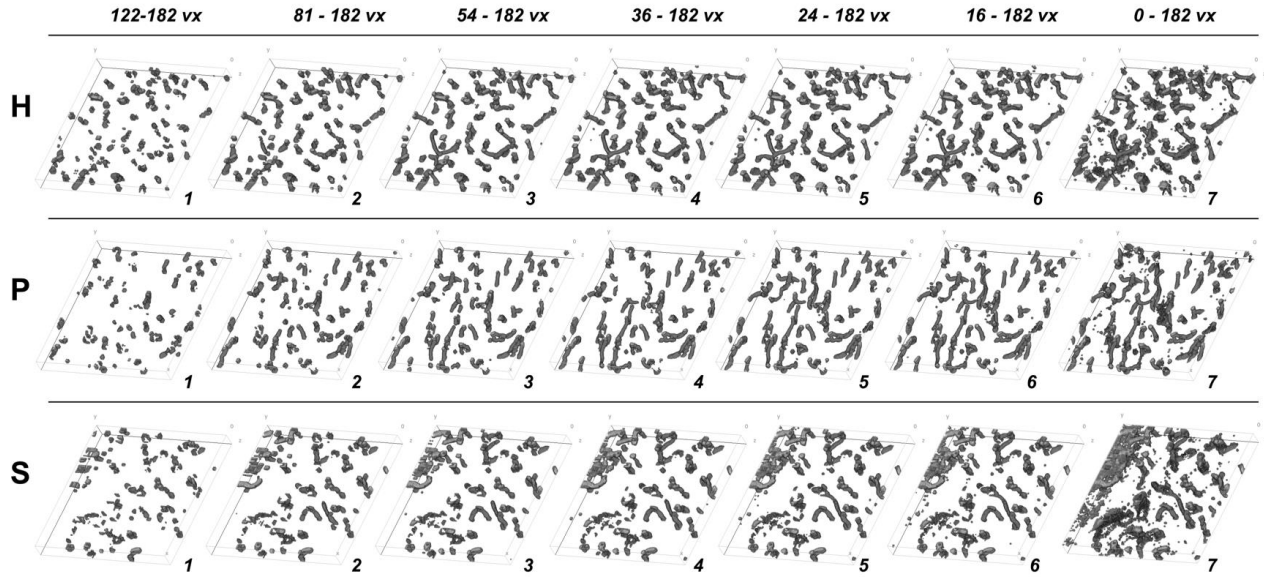

Figure 3 - Example of construction of analytical samples. A cervical spinal cord sample from a healthy (**H**), a pre-symptomatic (**P**) and a symptomatic (**S**) animal were caliber classified according to Set A thresholds. Signals from largest class are shown as volume views as PRA 1 at left. Additional PRA (2 to 7) were obtained adding signals from lower and lower caliber classes to obtain final PRA 7. Only these PRA signals were subjected to analysis.

PRAs provided the real samples to be analyzed, once they are normalized in terms of amount of input signal. In this respect, it is important to underscore that, for every sample, our signal dispersion analysis add new signals in a rhombicubocthahedron pattern around already existent voxels, up to reach the approximated amount of the largest sample observed[31,40]. At this point, the analysis starts to record the spatial dispersion of the sample, that is thus normalized according to the largest sample in the analysis.

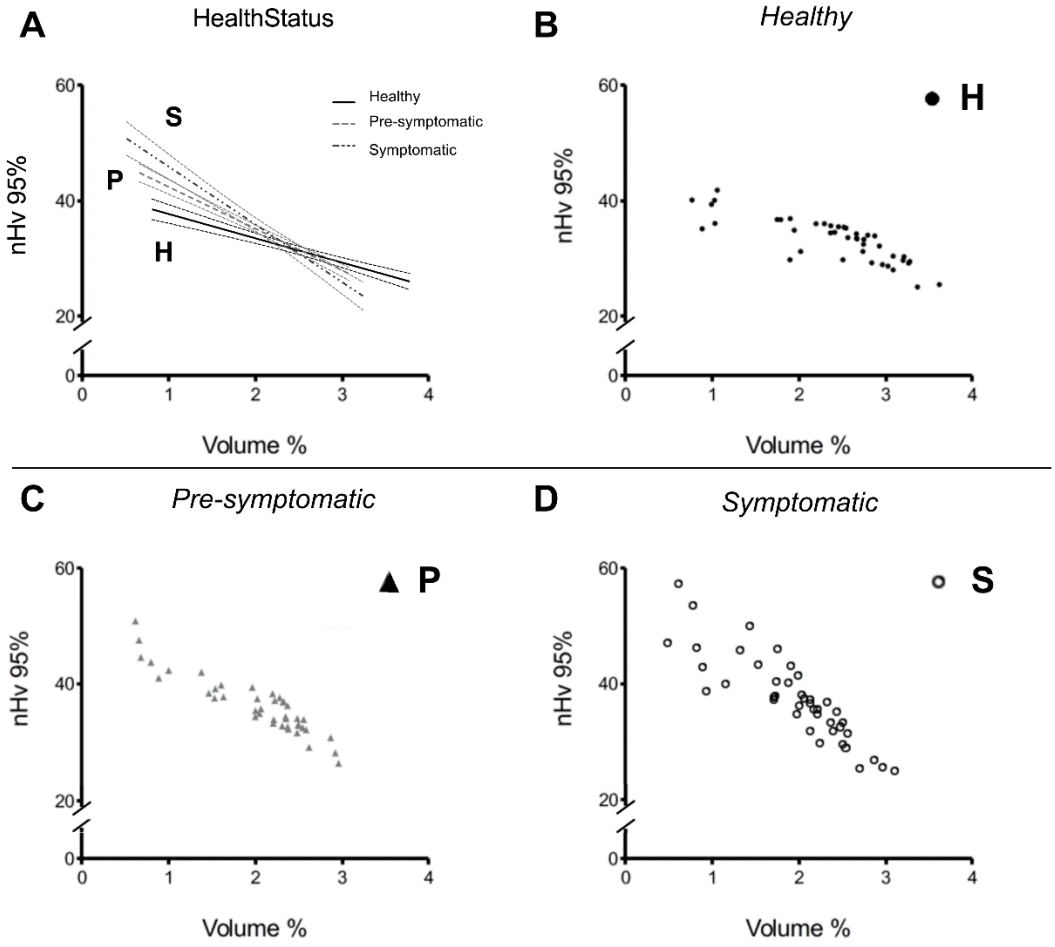

Figure 4 - Spinal cord analyses. Panel A summarizes linear regression lines obtained from spinal cord PRA from animals showing 3 different health conditions. Solid black line refer to Healthy (**H**) samples, dotted dark grey to pre-symptomatic (**P**) data and broken light grey to symptomatic values (**S**). Accompanying lines refer to 95% confidence limits for regression lines whose slope might seem to correlate with disease severity. However, absence of inter-animal variabilities spoiled results of biological meanings other than the ability of the test to highlight differences. Panels **B**, **C** and **D** detail point distribution and highlight variances.

Amount and Volume Dispersion Analysis of Normalized PRA

Concerned with signal reproducibilities, we tested angioarchitectures grouping them only by genetic background and by pathological symptoms. In this respect, we used together all 6 sets of PRAs coming from a single animal. They were derived from a healthy (H), a pre-symptomatic (P) or a symptomatic (S) swine, but in this preliminary work we tested only one animal for condition. In addition, at first we did not consider differences in ages as well as the different origin of samples from cervical, thoracic and lumbar districts of the spinal cord. Results were plotted in 2D graphs (Figure 4) according to percent signal amount of PRAs, on the X axis. Instead, the Y dimension reported for each point the normalized number of expansion cycles needed to fill-up 95% of the volume (nHv 95% index). Strikingly, even the control animal presented marked variability in spatial dispersion; it resulted larger than variability among contralateral samples derived from the same spinal cord district (data not

shown). In spite of this, health-status dependent LR presented different slopes, suggesting the possibility that the overall micro-angioarchitecture might be altered according to pathological condition.

Pathological samples show defined differences

Presented with regional specificity of spinal cord angioarchitectures we needed to re-consider data according to this new source of variability. Therefore, Figure 5 details results according to both pathological status and spinal cord district of source. The first column groups data to highlight differences in health status according to spinal district. Plots identify spinal regions as source of LR, but indicate also contributes from Healthy, Pre-symptpmatic and Symptomatyc animals through a capital letter. Conversely, first row details changes in angioarchitecture according to health status. In each graph, source of variability can be traced to contralateral volumes from the same animal, although the younger pre-symptomatic swine might present results not comparable because of its age (≈22 months in respect to ≈32-35 months for older animals). Here again, each LR trace is identified by a capital letter as derived from Cervical, Thoracic or Lumbar districts.

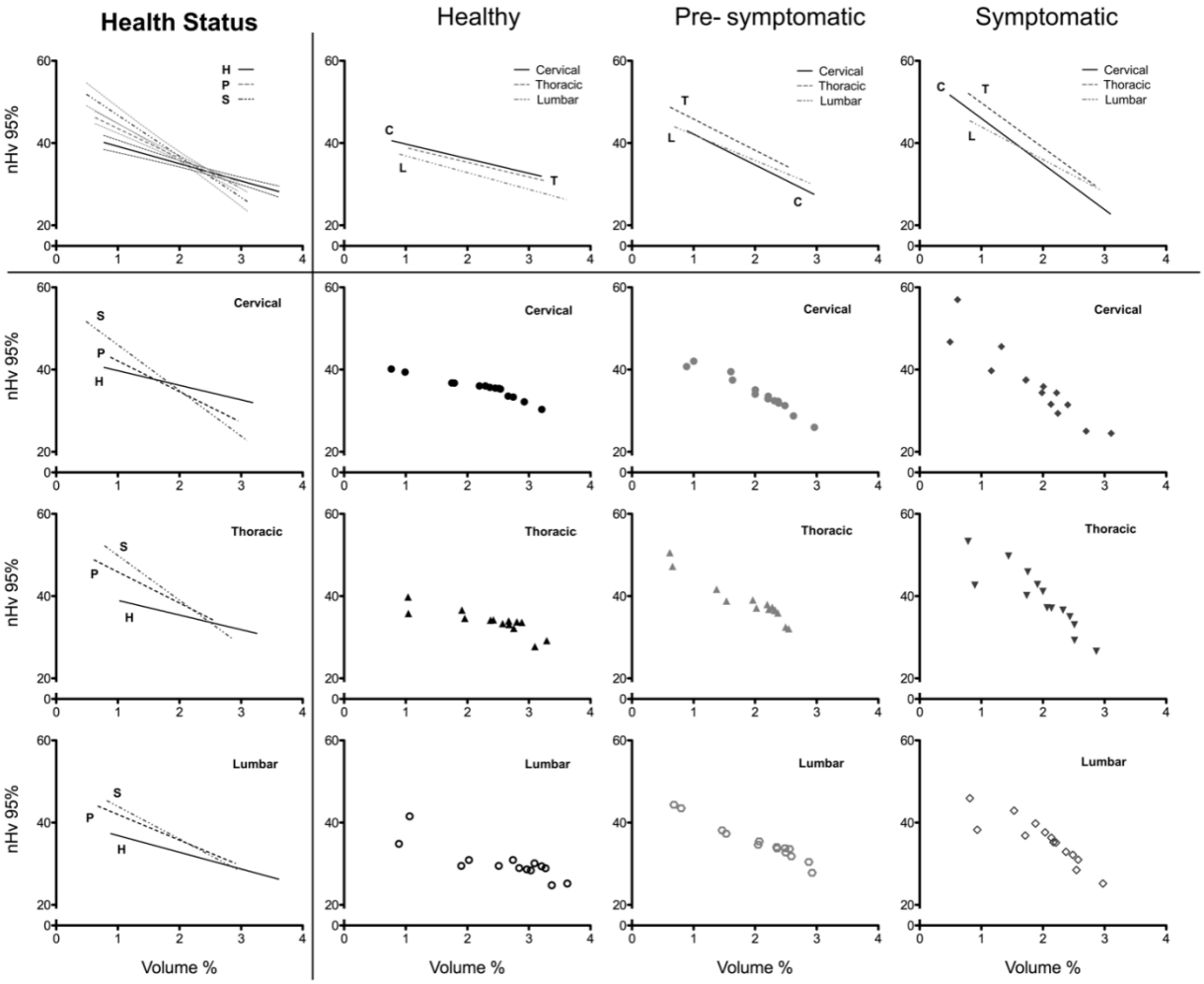

Figure 5 - Vascularization analysis by health status and spinal cord district. Figure is arranged as a 4x4, graphical table. At top-left, it presents the same Panel A of Figure 4 (n = 6 sets of PRA for each LR with their 95% confidence lines). Similarly, the top row of plots present contributes from Cervical (**C**), Thoracic (**T**) and Lumbar (**L**) signals for each of the **H**ealthy, **P**re-symptomatic or **S**ymptomatic animals (n = 2 sets for each LR). Then, in the first column at left, results are re-grouped according to which spinal district was being used as source of vascularization (n = 2 sets for each LR), among cervical, thoracic and lumbar regions. Plots arranged 3x3 in the bottom-right portion of the Figure, present data arrangements as derived from a single animal and a single district but showing lateral variability (n = 2 sets for each plot).

The absence of inter-animal variabilities spoiled our results of significance with respect to pathology. However, each animal appeared well-characterized. As a matter of fact, the healthy swine presented flatter representative regressions in cervical, thoracic and lumbar tissues with respect to others. Conversely, it confirmed the ability of the approach we used to identify and parametrize vascular differences in an ALS, swine model engineered to present a pre-symptomatic silent phase of the disease. Differences could be spotted for the 3 animals among cervical, thoracic and lumbar vessels. Here, signals appeared larger and loss of vascularization less pronounced than appropriate controls. No biological implications could be drawn, apart from the presence of differences in spinal cord angioarchitectures according to the regional origin of a sample. Nevertheless, this initial observation clarified methodological doubts, and pushed forth for an exhaustive analysis of the model, suggesting to control animal age as an additional variable.

Discussion

Dealing with neurological studies, innovation always raise outstanding expectations. Even considering only diagnosis, one would always expect that an additional biomarker, a new physical instrument, a new probe, might provide relevant results and contribute to objective diagnoses or unravelling of neurological diseases.

According to this vision, in this work we tried to clarify whether an approach found to work on brain tissues might be extended to spinal cord angioarchitectures and to samples reduced from near cubes to no more than thin slices. This work was preliminar to the study of the development of pathological symptoms in a swine animal model[14] of ALS, tuned to appear similar to what is known to happen in humans[13]. In our approach, we relied on the possibility to analyze microangioarchitectures on the basis of amount and spatial dispersion of microvascular signals classified according to their calibers[31,33,40]. We aimed to compare microangioarchitectures as single items, ranking them according to their potential functional proficiency. They were compared for potential ability in providing blood and cargo (higher caliber signals); similarly we tested them for potential cargo release (lower caliber signals) up to 95% of the tissue volume under analysis. In our conditions, we were analyzing only a tiny fraction of all vascular calibers, down to the smallest. On the other side, these vessels are those called to react to changing needs in the surrounding tissues[41], such as O_2 shortages or changes in hypoxia-inducible factor 1 alpha expression. Although this approach is demonstrated sound and useful in other contexts[31,33], here we doubted whether a difficult analytical set-up could not mask or alter the dispersion of larger vessels, preventing us to differentiate samples. Apparently, results solved our doubts, allowing us to identify differences in vascularization according to health status and to sources of samples. Further investigation must now clarify the possibility to repeat observations in different animals as well as the role of vascular changes in this neuropathological ALS model.

A second general advantage of the approach that might be worth to stress, is related to its basics. The approach itself is built upon construction of 3D Euclidean Distance Maps following rhombicubocthahedron dilations of calibered vascular signals. Thus, at a difference with Artificial Intelligence[42], the use of Euclidean geometry allowed us to split, or dilute in time, the automatic analytical process. In our effort, every intermediate result presented a logic meaning, could be tested or investigated, and might be saved to be possibly re-used in the context of other analyses. Furthermore, our analysis was immediately available (no need for computer training) and was totally reproducible. Obviously, we feel that a correctly trained Deep Learning network can provide superior results in much less time[43], once you know how to train it.

At biological level, we analyzed a low number of animals. This prevented us to draw correlations between the observed microangioarchitectures and the pathological state of the animals themselves. Although available data provide a "tantalizing" observation, we were unable to check for inter-animal variability and results might be interpreted in multiple ways. As a matter of fact, absence of replicated analyses spoiled the significance of our results on a pathological ground. In spite of this, the consistency of the results obtained within each animal supported the feasibility of the approach. It allowed to identify differences in the vascularization of spinal cord districts, repeating observations in animals at different pathogenetic stages. This is scarcely a surprise, given that different districts present different structures, both in terms of neuronal bodies and terminal axons[44], together with abundance of glial, endothelial[45] and mesenchimal cells[46]. However, it pointed out the possibilities of image analysis tools in the study of neuropathology.

The possible involvement of altered vascular networks in the development of ALS should not appear as extraordinary, and a recent study[17] demonstrates its importance. It is now well confirmed that neurodegenerative diseases such as Alzheimer's Disease[27], Parkinson's Disease[29] or Multiple Sclerosis[30] correlate with alterations in vascular districts, as it has been shown in retinal vasculature in human patients. These vascular plexa are particular important because images of retinal vascular angioarchitectures can be derived from human eyes using low-invasive techniques such as angio-Optical Coherence Tomography (angio-OCT)[26]. Studies are now progressing in this field, and in a far-fetched vision it might be possible to imagine to investigate for the neurological health of a patient by simple angio-OCT. Returning to the ALS model we used, the presence of a pre-symptomatic lag phase raises the question whether we will be able to confirm vascular alterations in spinal cords of pigs, notwithstanding the absence of motor symptoms. If this will be confirmed, the next question will regard the possibility to spot angio-OCT differences in retinal plexa of pre-symptomatic human ALS patients.

Conclusion

We observed that our semi-automatic image analysis approach can identify vascular alterations in spinal cord samples from a swine ALS model. In this pathology, our data focus attention to alterations in blood vessels microangioarchitectures, even if we were not yet able to demonstrate a direct correlation with disease progression.

Conflicts of Interest Statement

The authors have no conflicts of interest to declare.

Funding Statement

This work was partially funded by Project "InterSLA", ID 1157625 financed by Regione Lombardia and The Italian Consiglio Nazionale delle Ricerche (CNR) through the "Accordo per la Ricerca e l'Innovazione" initiative, in the framework of FESR: Fondo Europeo di Sviluppo Regionale.

Acknowledgements

We are indebted to:
Cristina Casalone, IZSTO Torino, Italy, for: suggestions and article proofreading
Sara Colombo, CNR-IN Milano, Italy for: local sample management and article proofreading.
Claudia Verderio, CNR-IN Milano, Italy, for: general project management and article proofreading.

References

1. Brown RH, Al-Chalabi A. Amyotrophic lateral sclerosis. *NEJM*. 2017; **377**:162-172. doi: 10.1056/NEJMra1603471.
2. Andersen PM. Amyotrophic lateral sclerosis associated with mutations in the CuZn superoxide dismutase gene. *Curr Neurol Neurosci Rep*. 2006; **6**:37–46. doi: 10.1007/s11910-996-0008-9.
3. Rosen DR, Siddique T, Patterson D, *et al*. Mutations in Cu/Zn superoxide dismutase gene are associated with familial amyotrophic lateral sclerosis. *Nature* 1993; **362**:59-62. doi: 10.1038/362059a0.
4. Turner BJ, Talbot K. Transgenics, toxicity and therapeutics in rodent models of mutant SOD1-mediated familial ALS. *Prog Neurobiol*. 2008; **85**:94–134. doi: 10.1016/j.pneurobio.2008.01.001.
5. Wu CH, Fallini C, Ticozzi N, *et al*. Mutations in the profilin 1 gene cause familial amyotrophic lateral sclerosis. *Nature*. 2012; **488**:499-503. doi: 10.1038/nature11280.
6. Zuo X, Zhou J, Li Y, *et al*. TDP-43 aggregation induced by oxidative stress causes global mitochondrial imbalance in ALS. *Nat Struct Mol Biol*. 2021; **28**(2):132-142. doi: 10.1038/s41594-020-00537-7.
7. Smith EF, Shaw PJ, De Vos KJ. The role of mitochondria in amyotrophic lateral sclerosis. *Neurosci Lett*. 2019; **710**:132933 doi: 10.1016/j.neulet.2017.06.052.
8. Leigh PN, Meldrum BS. Excitotoxicity in ALS. *Neurology*. 1996; **47**(6 Suppl 4):S221-7. doi: 10.1212/wnl.47.6_suppl_4.221s.
9. King AE, Woodhouse A, Kirkcaldie MT, Vickers JC. Excitotoxicity in ALS: Overstimulation, or overreaction? *Exp Neurol*. 2016; **275**:162-71. doi: 10.1016/j.expneurol.2015.09.019.
10. Peviani M, I Caron, C Pizzasegola, F Gensano, M Tortarolo, C Bendotti. Unraveling the complexity of amyotrophic lateral sclerosis: recent advances from the transgenic mutant SOD1 mice. *CNS Neurol Disord Drug Targets* 2010; **9**:491–503. doi: 10.2174/187152710791556096.
11. Sreedharan J, Blair IP, Tripathi VB, *et al*. TDP-43 mutations in familial and sporadic amyothropic lateral sclerosis. *Science* 2008; **319**:1668-1672. doi: 10.1126/science.1154584.
12. Perrin S. Preclinical research: make mouse studies work. *Nature* 2014; **507**:423–425. doi: 10.1038/507423a.
13. Oskarsson B, Gendron TF, Staff NP. Amyotrophic Lateral Sclerosis: An Update for 2018. *Mayo Clin Proc*. 2018; **93**:1617-1628. doi: 10.1016/j.mayocp.2018.04.007.
14. Crociara P, Chieppa MN, Costassa EV, *et al*. Motor neuron degeneration, severe myopathy and TDP-43 increase in a transgenic pig model of SOD1-linked familiar ALS *Neurobiol Dis*. 2019; **124**:263-275. doi: 10.1016/j.nbd.2018.11.021.
15. Eisen A. Response to a letter by Dr T Ramesh. *J Neurol. Neurosurg Psychiatry*. 2014; **85**:1289. doi: 10.1136/jnnp-2014-308588.
16. Talbot K. Amyotrophic lateral sclerosis: cell vulnerability or system vulnerability? *J Anat*. 2014; **224**:45–51. doi: 10.1111/joa.12107.
17. Månberg A, Skene N, Sanders F, *et al*. Altered perivascular fibroblast activity precedes ALS disease onset. *Nature Med*. 2021; **27**:640-646. doi: 10.1038/s41591-021-01295-9.
18. Guo M, Hao Y, Feng Y, *et al*. Microglial Exosomes in Neurodegenerative Disease. *Front Mol Neurosci*. 2021; **14**:630808. doi: 10.3389/fnmol.2021.630808.
19. Lewandowski SA, Nilsson I, Fredriksson L, *et al*. Presymptomatic activation of the PDGF-CC pathway accelerates onset of ALS neurodegeneration. *Acta Neuropathol*. 2016; **131**:453-464. doi: 10.1007/s00401-015-1520-2.
20. Zhong Z, Deane R, Ali Z, *et al*. ALS-causing SOD1 mutants generate vascular changes prior to motor neuron degeneration. *Nat. Neurosci*. 2008; **11**:420-422. doi: 10.1038/nn2073.
21. Ehling J, Theek B, Gremse F, *et al*. Micro-CT Imaging of Tumor angiogenesis quantitative measures describing micromorphology and vascularization. *Am J Pathol*. 2014; **184**:431-441. doi: 10.1016/j.ajpath.2013.10.014.
22. Helmberger M, Pienn M, Urschler M, *et al*. Quantification of tortuosity and fractal dimension of the lung vessels in pulmonary hypertension patients. *PLoS ONE* 2014; **9**:e87515 doi: 10.1371/journal.pone.0087515.
23. Scott A Powner MB, Fruttiger M. Quantification of vascular tortuosity as an early outcome measure in oxigen induced retinopathy (OIR). *Exp Eye Res*. 2014; **120**:55-60 doi: 10.1016/j.exer.2013.12.020.
24. Di Ieva A, Grizzi F, Ceva-Grimaldi G, *et al*. Fractal dimension as a quantitator of the microvasculature of normal and adenomatous pituitary tissue. *J Anat*. 2007; **211**:673-680. doi: 10.1111/j.1469-7580.2007.00804.x.
25. Van Craenendonck T, Gerrits N, Buelens B, *et al*. Retinal microvascular complexity comparing mono- and multifractal dimensions in relation to cardiometabolic risk factors in a Middle Eastern

population. *Acta Ophthalmol*. 2021; **99**:e368-e377. doi: 10.1111/aos.14598.

26. Wang L, Murphy O, Caldito NG, Calabresi PA, Saidha S. Emerging applications of Optical Coherence Tomography Angiography (OCTA) in neurological research. *Eye Vis. (Lond)* 2018; **5**:11-22 doi: 10.1186/s40662-018-0104-3.

27. O'Bryhim BE, Apte RS, Kung N, Coble D, Van Stevern GP. Association of Preclinical Alzheimer Disease with Optical Coherence Tomography Angiography Findings. *JAMA Ophthalmology* 2018; **136**:1242-1248. doi: 10.1001/jamaophthalmol.2018.3556.

28. Sorrentino FS, Matteini S, Bonifazzi C, Sebastiani A, Parmeggiani F. Diabetic retinopathy and endothelin system: microangiopathy versus endothelial dysfunction. *Eye (Lond)* 2018; **32**:1157-1163. doi: 10.1038/s41433-018-0032-4.

29. Kwapong WR, Ye H, Peng C, *et al*. Retinal Microvascular Impairment in the Early Stages of Parkinson's Disease. *Invest Ophthalmol Vis. Sci*. 2018; **59**:4115-4122. doi: 10.1167/iovs.17-23230.

30. Britze J, Frederiksen JL. Optical coherence tomography in multiple sclerosis *Eye (Lond)* 2018; **32**:884-888 doi: 10.1038/s41433-017-0010-2.

31. Righi M, Locatelli SL, Carlo-Stella C, Presta M, Giacomini A. *Sci. Rep*. 2018; **8**:7520-17531. doi: 10.1038/s41598-018-35788-4.

32. Namba M, Oktsuki T, Mori M, *et al*. Establishment of five human myeloma cell lines. *In Vitro Cell Dev Biol*. 1989; **25**:723-729. doi: 10.1007/BF02623725.

33. Righi M, Belleri M, Presta M, Giacomini A. Quantification of 3D brain micro-angioarchitectures in an animal model of Krabbe Disease. *IJMS* 2019; **20**:2384-2398 doi: 10.3390/ijms20102384.

34. Giacomini A, Ackermann M, Belleri M, *et al*. Brain angioarchitecture and intussusceptive microvascular growth in a murine model of Krabbe Disease. *Angiogenesis* 2015; **18**:499-510. doi: 10.1007/s10456-015-9481-6.

35. Carol A, Graziano E, Cardile V. History, genetic, and recent advances on Krabbe Disease. *Gene* 2015; **555**: 2-13. doi: 10.1016/j.gene.2014.09.046.

36. Chieppa MN, Perota A, Corona C, *et al*. Modeling amyotrophic lateral sclerosis in hSOD1 transgenic swine. *Neurodegener Dis*. 2014; **13**:246–254. doi: 10.1159/000353472.

37. Robertson RT, Levine ST, Haynes SM, *et al*. Use of labeled tomato lectin for imaging vasculature structures. *Histochem Cell Biol*. 2015; **143**:225-34. doi: 10.1007/s00418-014-1301-3.

38. Schneider CA, Rasband WS, Eliceiri KW. NIH Image to ImageJ: 25 years of image analysis. *Nature Methods* 2012; **9**:671-675. doi: 10.1038/nmeth.2089.

39. Righi M, Presta M, Giacomini A. Quantification of Tumor Vasculature by Analysis of Amount and Spatial Dispersion of Caliber-Classified Vessels. *Methods Mol Biol*. 2021; **2206**:151-178. doi: 10.1007/978-1-0716-0916-3_12.

40. Carlo-Stella C, Locatelli SL, Giacomini A, *et al*. Sorafenib inhibits lymphoma xenografts by targeting MAPK/ERK and AKT pathways in tumor and vascular cells. PLoS ONE. 2013; **8**(4):e61603. doi: 10.1371/journal.pone.0061603.

41. Korbecki J, Simińska D, Gąssowska-Dobrowolska M, *et al*. Chronic and Cycling Hypoxia: Drivers of Cancer Chronic Inflammation through HIF-1 and NF-κB Activation: A Review of the Molecular Mechanisms. *Int J Mol Sci*. 2021; **22**:10701. doi: 10.3390/ijms221910701.

42. LeCun Y, Bengio Y, Hinton G. Deep Learning. *Nature* 2015; **521**:436-444. doi: 10.1038/nature14539.

43. Kermany DS, Goldbaum M, Cai W, *et al*. Identifying Medical Diagnoses and Treatable Diseases by Image-Based Deep Learning. Cell 2018; **172**:1122-1131. doi: 10.1016/j.cell.2018.02.010.

44. Bogduck Nikolai. Functional anatomy of the spine. *Handb Clin Neurol*. 2016; **136**:675-88. doi: 10.1016/B978-0-444-53486-6.00032-6.

45. Kashima TG, Dongre A, Athanasou NA. Lymphatic involvement in vertebral and disc pathology. *Spine* (Phila Pa 1976). 2011; **36**:899-904. doi: 10.1097/BRS.0b013e3182050284.

46. Arkesteijn ITM, Smolders LA, Spillekom S, *et al*. Effect of coculturing canine notochordal, nucleus pulposus and mesenchymal stromal cells for intervertebral disc regeneration. *Arthritis Res Ther*. 2015; **17**:60-72. doi: 10.1186/s13075-015-0569-6.